



Cite this: *Nanoscale*, 2018, **10**, 5442

Received 28th December 2017,
 Accepted 19th February 2018

DOI: 10.1039/c7nr09682h

rsc.li/nanoscale

Holey nickel hydroxide nanosheets for wearable solid-state fiber-supercapacitors†

Peipei Shi,^{‡a} Rong Chen,^{‡b} Li Li,^a Jianing An,^c Li Hua,^a Jinyuan Zhou,^{id d} Bin Liu,^{*b} Peng Chen,^{id *b} Wei Huang^{a,e} and Gengzhi Sun^{id *a}

Holey nickel hydroxide (Ni(OH)₂) nanosheets with a mean thickness of 2 nm are facilely synthesized, and then embedded in carbon nanotube (CNT) scaffolds to construct a hybrid fiber electrode, which shows a high volumetric capacitance of 335.9 F cm⁻³ at 0.8 A cm⁻³ and superior rate performance. The hybrid supercapacitor made from the Ni(OH)₂/CNT fiber can deliver a high specific capacitance of 24.8 F cm⁻³ and an energy density of 5.8 mW h cm⁻³ with outstanding mechanical stability under repeated bending conditions.

With the rapid development of flexible and wearable electronic devices, there are increasing demands for compatible energy storage systems that are lightweight, flexible, and even weavable.^{1–9} A fiber-shaped supercapacitor is considered as one of the most promising candidates to power wearable electronic devices,¹⁰ which has already been successfully demonstrated based on a number of fibrous materials, *e.g.*, metallic wires,¹¹ carbon fibers (CFs),¹² graphene fibers¹³ and carbon nanotube (CNT) fibers.¹⁴ However, the critical challenge in fiber-shaped supercapacitors remains to be their low energy density. Based on the equation $E = \frac{1}{2}CV^2$ (where E , C , and V represent energy density, capacitance, and cell voltage, respectively), E is determined by the capacitance of the fiber electrode as well as the cell voltage, which can be widened *via* an asymmetric device design.^{15–18}

A common strategy to increase the capacitance of the fiber electrode is to incorporate electrochemically active materials with conductive filaments (*e.g.*, carbonaceous fibers) using, for example, hydrothermal or electrochemical deposition to form a core-shell structure.^{19–23} Although the active materials offer enlarged capacitance, the performance of the fiber electrodes is still far away from satisfactory. The critical issues include: (1) often only the shell is active while the bulk core of the fiber does not participate in the electrochemical charge-discharge processes,^{24–26} and (2) the shell active material is not efficiently utilized due to its poor conductivity, thus the loading capacity of the active material is limited.²⁴ Therefore, the areal/volumetric capacitances and rate capability of the hybrid fiber electrode are significantly compromised. Moreover, owing to the rigidity and brittleness of the shell active materials, the mechanical robustness of the hybrid fiber is poor.²⁷ As a step forward, microstructural design of hybrid fibers has been demonstrated as a promising strategy to achieve the synergistic interaction between conductive filaments and active nanomaterials. Recently, an amorphous MnO₂@CNT fiber was developed, in which the homogeneously dispersed MnO₂ nanoparticles offer high pseudocapacitance while the CNT scaffold provides the hybrid fiber with good electrical conductivity and mechanical robustness.²⁸ This hybrid fiber electrode exhibited improved rate performance compared to the core-shell counterparts, whereas due to the low theoretical capacitance and the loading amount of MnO₂ nanoparticles, the fiber performance remains unsatisfactory. Ideally, the active materials should be of low resistance, large accessible surface area, high theoretical capacitance, earth abundance and non-toxicity, for instance Ni(OH)₂.^{26,29–38}

In this study, ultrathin Ni(OH)₂ nanosheets with a holey structure and small lateral sizes were successfully synthesized by a fast-precipitation method, and then the as-prepared nanosheets were incorporated into an interconnected and well-aligned carbon nanotube (CNT) scaffold using a scrolling method to obtain highly flexible Ni(OH)₂/CNT fibers.³⁹ Owing to the thin thickness, small lateral size and the holey structure of Ni(OH)₂ nanosheets, the excellent mechanical and electrical

^aKey Laboratory of Flexible Electronics (KLOFE) & Institute of Advanced Materials (IAM), Jiangsu National Synergetic Innovation Center for Advanced Materials (SICAM), Nanjing Tech University (NanjingTech), 30 South Puzhu Road, Nanjing 211816, P. R. China. E-mail: iamgzsun@njtech.edu.cn

^bSchool of Chemical and Biomedical Engineering, Nanyang Technological University, 62 Nanyang Drive, 637459, Singapore. E-mail: ChenPeng@ntu.edu.sg, liubin@ntu.edu.sg

^cSchool of Mechanical and Aerospace Engineering, Nanyang Technological University, 50 Nanyang Avenue, 639798, Singapore

^dSchool of Physical Science and Technology, Lanzhou University, 222 South Tianshui Road, Lanzhou 730000, Gansu, P. R. China

^eShaaxi Institute of Flexible Electronics (SIFE), Northwestern Polytechnical University, 127 West Youyi Road, Xi'an 710072, P. R. China

†Electronic supplementary information (ESI) available. See DOI: 10.1039/c7nr09682h

‡These authors contribute equally to this work.

properties of the CNT scaffold, as well as the unique microstructure of the hybrid fiber, the Ni(OH)₂/CNT fiber electrode exhibited an optimal volumetric capacitance of 335.9 F cm⁻³ at 0.8 A cm⁻³ with excellent rate performance, retaining 81.5% of the initial capacitance at a charge–discharge current density of 8.0 A cm⁻³. The Ni(OH)₂/CNT fiber was further utilized as the positive electrode to construct a wearable solid-state hybrid supercapacitor, which could deliver a high specific capacitance of 24.8 F cm⁻³ at 1.0 A cm⁻³ and an energy density of 5.8 mW h cm⁻³ at a power density of 0.6 W cm⁻³ with outstanding mechanical stability.

Holey Ni(OH)₂ nanosheets were prepared based on a facile fast-precipitation method similar to our previous study.⁴⁰ The thickness of Ni(OH)₂ nanosheets was found to be ~2 nm by atomic force microscopy (AFM) (Fig. S1†). The as-prepared Ni(OH)₂ nanosheet ink in ethanol at a concentration of 1 mg mL⁻¹ had a zeta potential of 61.99 mV (Fig. S2†), and is highly stable without any precipitation for more than one month (Fig. 1a). The crystal structure of the Ni(OH)₂ nanosheets was characterized by X-ray diffraction (XRD). As

shown in Fig. 1b, the diffraction peaks at 19.32, 33.06, 38.90, 52.08, 59.06, and 62.68° can be well ascribed to the diffractions of the (001), (100), (101), (102), (110), and (111) planes of β-Ni(OH)₂ (JCPDS: 14-0117). Fig. 1c displays a typical transmission electron microscopy (TEM) image of the Ni(OH)₂ nanosheets, which clearly illustrates the ultrathin feature of the nanosheets with an average lateral size of ~34 nm. In addition, the high-resolution TEM (HRTEM) image (Fig. 1d) reveals the holey microstructure of Ni(OH)₂ nanosheets, which was further evidenced by the N₂ adsorption/desorption isotherms (Fig. 1e); the specific surface area of the Ni(OH)₂ nanosheets is 95 m² g⁻¹. The average pore size is about 10 nm (Fig. 1f), which is in good agreement with the TEM observation.

The as-prepared Ni(OH)₂ nanosheets were incorporated into an interconnected and well-aligned CNT scaffold to obtain highly flexible Ni(OH)₂/CNT hybrid fibers. Owing to the intimate interaction between CNTs, a highly-aligned CNT film could be continuously pulled out from the vertical CNT array, which was grown by chemical-vapor deposition (Fig. S3†).^{41–43} As schematically shown in Fig. 2a, four layers of the CNT films (width of *ca.* 1.6 mm and a length of *ca.* 7 cm) were stacked and then laid on a polytetrafluoroethylene (PTFE) substrate. The Ni(OH)₂ nanosheets dispersed in ethanol were drop-cast on the stacked CNT film. The loading amount of Ni(OH)₂ nanosheets could be readily adjusted by repeating the casting cycles. The resulting hybrid film was peeled off the PTFE substrate, and subsequently scrolled into a hybrid fiber (Ni(OH)₂/CNT fiber) by using an electric motor at a rotating speed of 200 rpm for 3 min. The CNTs in the hybrid fiber maintained their good alignment (Fig. 2b). The energy dispersive X-ray spectroscopy (EDS) spectra (Fig. 2b) display a homogeneous

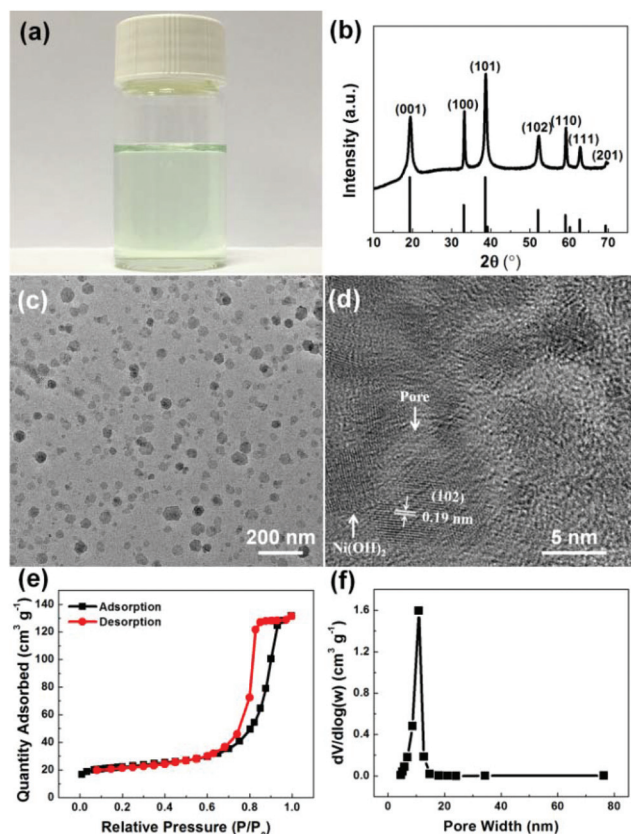


Fig. 1 (a) Photograph of Ni(OH)₂ nanosheets that are uniformly dispersed in ethanol at a concentration of 1 mg mL⁻¹. (b) XRD pattern of the as-prepared Ni(OH)₂ nanosheets. (c) TEM image of holey Ni(OH)₂ nanosheets. (d) HRTEM image of the Ni(OH)₂ nanosheet. The marked lattice distance of 0.19 nm can be assigned to the (102) plane. (e) N₂ adsorption/desorption isotherms and (f) the corresponding pore size distribution of Ni(OH)₂ nanosheets.

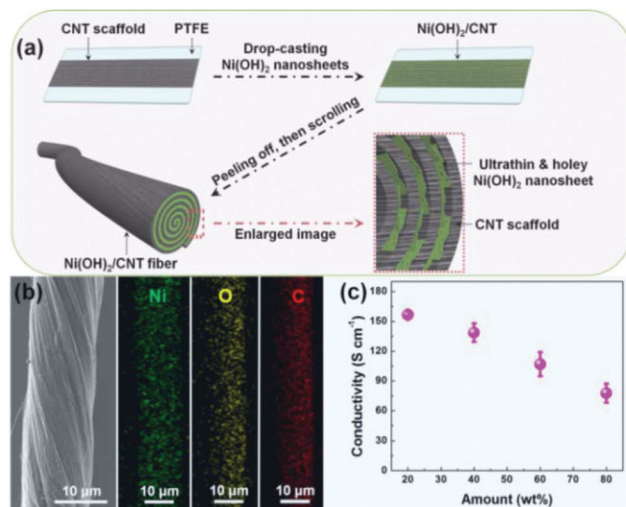


Fig. 2 (a) Schematic illustration showing the fabrication of the Ni(OH)₂/CNT hybrid fiber. (b) SEM image and EDS mapping of the Ni(OH)₂/CNT hybrid fiber. (c) The conductivity of the Ni(OH)₂/CNT hybrid fiber with different loading amounts of Ni(OH)₂ nanosheets (20, 40, 60 and 80 wt%). The statistics was obtained from 3 samples for each data point.

distribution of the Ni, O and C elements across the entire hybrid fiber, indicating that Ni(OH)₂ nanosheets were homogeneously incorporated into the helical corridors in the twisted CNT filaments. Because of the porous feature of the CNT scaffold, the embedded Ni(OH)₂ nanosheets with a high specific surface area can be easily accessible by electrolytic ions, while at the same time the well-aligned CNT scaffold provides the hybrid fiber with good mechanical robustness and a fast electron transport pathway. In contrast to commercial carbon fibers, the Ni(OH)₂/CNT hybrid fiber exhibits high flexibility and can be easily knotted (Fig. S4†). The conductivity of the Ni(OH)₂/CNT fiber was measured as a function of the loading amounts of holey Ni(OH)₂ nanosheets. The bare CNT fiber shows a conductivity of 204 S cm⁻¹, which slowly decreases with the increase in the loading of Ni(OH)₂ nanosheets (Fig. 2c).

The electrochemical performance of the Ni(OH)₂/CNT hybrid fiber electrode was evaluated by cyclic voltammetry (CV) and galvanostatic charge–discharge (GCD) measurements in a three-electrode configuration in 1 M KOH solution. Pt foil and Ag/AgCl (in saturated KCl solution) were used as the counter and reference electrodes, respectively. The CV peaks (Fig. 3a) located at 0.45 and 0.28 V vs. Ag/AgCl correspond to the redox reaction between Ni(OH)₂ and NiOOH, following the reaction

of Ni(OH)₂ + OH⁻ = NiOOH + H₂O + e⁻.^{44–46} The maximum volumetric current density of the Ni(OH)₂/CNT fiber electrode was obtained with 40 wt% of Ni(OH)₂ loading. The CV curve of the Ni(OH)₂/CNT hybrid fiber (40 wt%) slightly distorted at 100 mV s⁻¹ compared to that measured at 5 mV s⁻¹ (Fig. S5†). The capacity was calculated in terms of specific volumetric capacitance (*C_v*, F cm⁻³) and gravimetric capacitance (*C_g*, F g⁻¹) based on the GCD measurements at different current densities as shown in Fig. 3b. The *C_g* calculated based on the mass of Ni(OH)₂ nanosheets reaches as high as 1201.4 F g⁻¹ at 5.0 A g⁻¹ for the Ni(OH)₂/CNT fiber with 20 wt% of Ni(OH)₂ nanosheets, demonstrating the effective utilization of Ni(OH)₂.^{47–49} With a further increase in the mass loading of Ni(OH)₂ nanosheets, *C_g* keeps decreasing, reaching 780.2 F g⁻¹ for the Ni(OH)₂/CNT fiber with 80 wt% of Ni(OH)₂ nanosheets due to increased charge transport resistance. By tuning the composition of the Ni(OH)₂/CNT fiber, the optimal *C_v* of 319.6 F cm⁻³ (at a current density of 2.0 A cm⁻³) could be obtained for the Ni(OH)₂/CNT fiber with 40 wt% of Ni(OH)₂ nanosheets. The GCD curves of the Ni(OH)₂/CNT fiber electrode with 40 wt% of Ni(OH)₂ nanosheets were measured at different current densities ranging from 0.8 to 8.0 A cm⁻³ (Fig. 3c), and the calculated *C_v* falls from 335.9 to 273.7 F cm⁻³ with a high capacitance retention of 81.5% (Fig. 3d). In addition, the Ni(OH)₂/CNT fiber electrode shows excellent electrochemical stability with a capacitance retention of 96.3% after 4000 charge–discharge cycles at 5.0 A cm⁻³ (Fig. S6†), and Ni(OH)₂ remained well hosted in the fiber which is evidenced by SEM imaging and EDS mapping (Fig. S7†). The high capacitance, excellent rate performance and cycling stability of the Ni(OH)₂/CNT fiber electrode can be ascribed to the following three factors (Fig. 3e): (1) Ni(OH)₂ has a high theoretical capacitance; (2) the interconnected and well-aligned CNT scaffold offers high mechanical strength and excellent electrical conductivity (Fig. 2c); and (3) the ultrathin and holey Ni(OH)₂ nanosheets provide large accessible active surface, allowing fast ion-transport as evidenced by the electrochemical impedance spectroscopy (EIS) measurement, in which the slope only changes slightly in the high frequency regime as compared to that of the bare CNT fiber electrode (Fig. S8†), indicating efficient ion transport. It is noteworthy that, to the best of our knowledge, the Ni(OH)₂/CNT fiber exhibits a record high capacitance (335.9 F cm⁻³ at 0.8 A cm⁻³), which is superior to the recently reported MnO₂/CNT fiber (154.7 F cm⁻³ at 2.3 A cm⁻²),⁵⁰ rGO/SWCNT fiber (210 F cm⁻³ at 0.75 A cm⁻³),⁵¹ PEDOT/CNT fiber (169 F cm⁻³ at 0.01 V s⁻¹)⁵² and rGO/CNT fiber (158 F cm⁻³ at 0.1 mA cm⁻²).⁵³

Using the same method, graphene oxide (GO) nanosheets could also be incorporated into the CNT scaffold with a GO loading amount of 90 wt%. After obtaining the GO/CNT fiber, GO was chemically reduced by hydroiodic acid (HI) to give the rGO/CNT fiber, which has a diameter of ~27 μm and is highly flexible and robust (Fig. 4a). The rGO/CNT fiber electrode was also electrochemically characterized in a three-electrode configuration using 1 M KOH solution as the electrolyte. As shown in Fig. 4b, the CV curve measured at

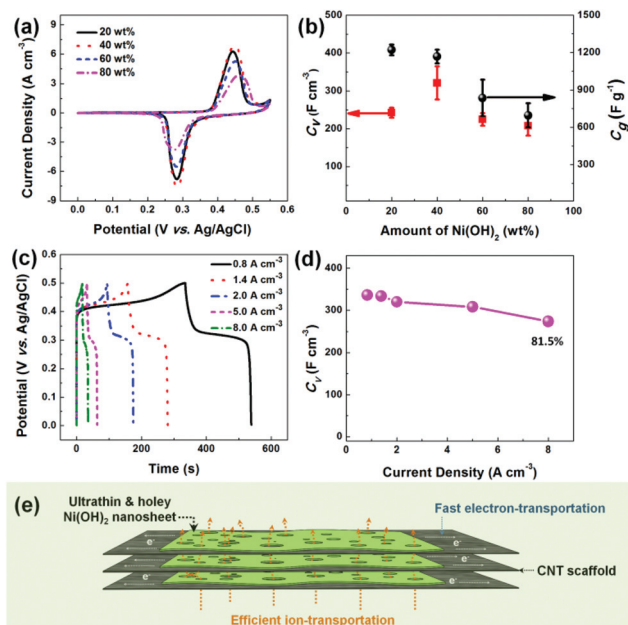


Fig. 3 (a) CV curves of the Ni(OH)₂/CNT hybrid fiber electrode with different loading amounts of Ni(OH)₂ nanosheets (20, 40, 60, and 80 wt%) at a scan rate of 5 mV s⁻¹ in 1 M KOH. (b) Volumetric capacitance (*C_v*) and gravimetric capacitance (*C_g*) of the Ni(OH)₂/CNT fiber electrode as a function of the loading amount of Ni(OH)₂ nanosheets, respectively. (c) Galvanostatic charge–discharge (GCD) curves of the Ni(OH)₂/CNT fiber electrode at current densities of 0.8, 1.4, 2.0, 5.0, and 8.0 A cm⁻³ with 40 wt% of Ni(OH)₂ nanosheets. (d) Current density dependent *C_v* of the Ni(OH)₂/CNT fiber electrode. (e) Schematic illustration showing the mechanism of efficient ion- and electron-transport.

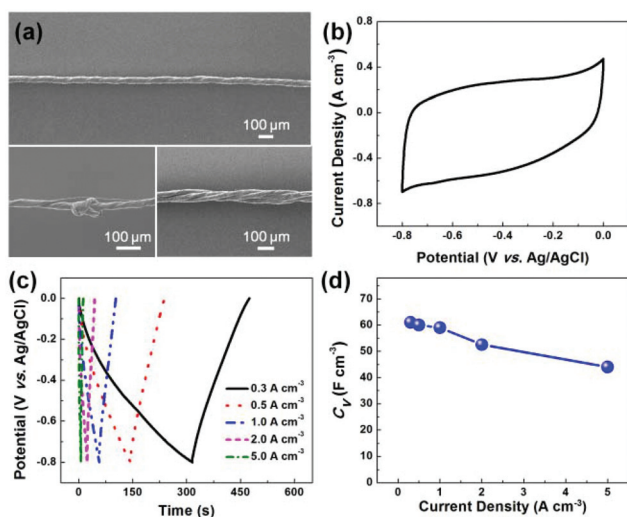


Fig. 4 (a) SEM image of the rGO/CNT fiber. (b) CV curve of the rGO/CNT fiber electrode with 90 wt% of rGO loading at a scan rate of 5 mV s^{-1} in 1 M KOH . (c) GCD curves of the rGO/CNT fiber electrode at current densities of 0.3, 0.5, 1.0, 2.0, and 5.0 A cm^{-2} . (d) Current density dependent C_V of the rGO/CNT fiber electrode.

5 mV s^{-1} is nearly rectangular within a potential window of 0 to -0.8 V . Based on the GCD curves measured at charge–discharge current densities from 0.3 to 5.0 A cm^{-2} (Fig. 4c), the C_V of the rGO/CNT fiber electrode decreased from 61.0 to 43.8 F cm^{-3} (Fig. 4d) with a capacitance retention of 71.8%.

Employing the $\text{Ni(OH)}_2/\text{CNT}$ fiber and the rGO/CNT fiber as the positive and negative electrode, respectively, the working voltage of the hybrid supercapacitor can reach as high as 1.3 V (Fig. 5a). The specific volumetric capacitance calculated from the GCD curves (Fig. 5b) at charge–discharge current densities ranging from 0.4 to 2.0 A cm^{-2} falls between 28.1 and 20.2 F cm^{-3} (Fig. 5c) with a capacitance retention of 71.9%. Fig. 5d shows the Ragone plot, which compares the performance of our hybrid supercapacitor with those recently reported in the literature.⁵⁴ The performance of our fiber-supercapacitor is superior to the commercial 63 V per $220 \mu\text{F}$ electrolytic capacitor⁵⁵ and 3 V per $300 \mu\text{F}$ Al electrolytic capacitor,⁵⁶ as well as the fiber-based supercapacitors such as CF@MnO_2 fibers,⁵⁷ $\text{MoS}_2\text{-rGO/CNT}$ fibers,¹⁴ MnO_2/CNT fibers,²⁸ PEDOT/CNT biscrolled yarn,⁵² CoAl LDH@CF ,⁵⁸ and $\text{Ni(OH)}_2/\text{Ni}$ fiber,⁵⁹ but slightly lower than $\text{Ni(OH)}_2/\text{CF}$.⁶⁰ Additionally, our hybrid supercapacitor, which was woven in a glove, exhibits excellent flexibility (Fig. 5e), and the hybrid device also demonstrates good cycling stability with a capacitance retention of 93.8% over 3000 cycles (Fig. 5f). The hybrid device does not show any capacitance fading even after 5000 bending–unbending cycles at a current density of 0.8 A cm^{-2} (Fig. S9†). As a demonstration of practical application, four hybrid supercapacitors were connected in series, which could be used to lighten up a red light emitting diode (LED) (Fig. S10†).

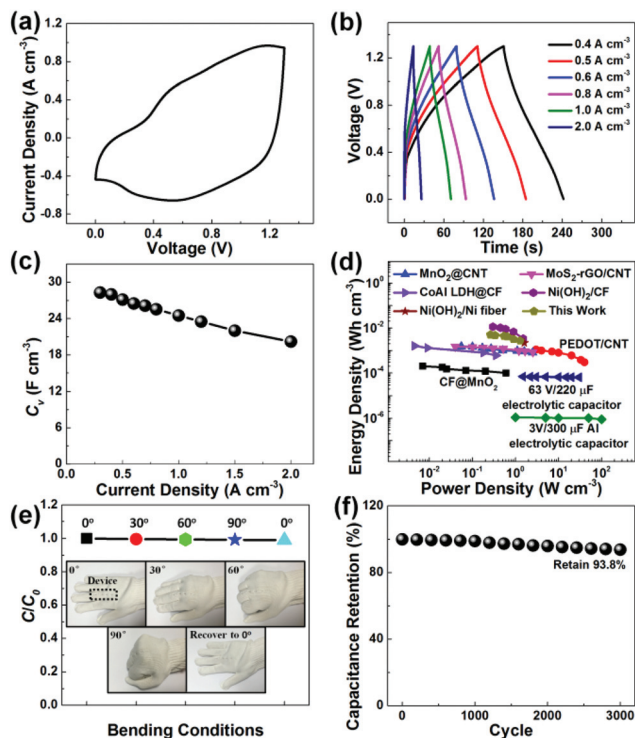


Fig. 5 (a) CV curve of the hybrid supercapacitor based on $\text{Ni(OH)}_2/\text{CNT}$ and rGO/CNT fiber electrodes at a scan rate of 5 mV s^{-1} . (b) GCD curves of the hybrid supercapacitor at current densities of 0.4 to 2.0 A cm^{-2} . (c) Current density dependent C_V of the hybrid supercapacitor. (d) Ragone plot to compare the volumetric energy density (E_V) and power density (P_V) with previously reported studies. (e) Performance of the fiber-shaped supercapacitor at different bending angles ($0^\circ\text{--}90^\circ\text{--}0^\circ$). (f) Cycling stability of the hybrid supercapacitor at a current density of 1.0 A cm^{-2} .

Conclusions

In summary, we have designed a superior fiber electrode based on ultrathin holey Ni(OH)_2 nanosheets embedded into an interconnected and well-aligned CNT scaffold. Thanks to the combined effects of the good mechanical and electrical properties of the CNT scaffold as well as the ultrathin and holey characteristics of Ni(OH)_2 nanosheets, the $\text{Ni(OH)}_2/\text{CNT}$ fiber exhibits high volumetric capacitance and excellent rate performance. The solid-state hybrid supercapacitor based on a $\text{Ni(OH)}_2/\text{CNT}$ fiber anode and an rGO/CNT fiber cathode was then fabricated and woven in a glove, which exhibited a wide voltage window with high capacitance and excellent flexibility. It is anticipated that the flexible fiber-supercapacitor fabricated in this work should benefit novel applications in wearable electronics.

Experimental section

$\text{Ni(NO}_3)_2 \cdot 6\text{H}_2\text{O}$ (99.9%, AR grade), NaOH (99.98%, AR grade), KOH (99.98%, AR grade) and ethanol ($\geq 99.7\%$) were purchased

from Shanghai Ling Feng Chemical Reagent Co., Ltd. Poly (vinyl alcohol) (PVA, MW 85 000 to 124 000) was obtained from Sigma-Aldrich. All chemicals were used as received.

The holey Ni(OH)₂ nanosheets were prepared using a fast-precipitation method similar to our previous study. Briefly, a solution containing 1.5 mmol of Ni(NO₃)₂ was quickly added into 20 mL of NaOH aqueous solution (0.15 M) under vigorous stirring. Subsequently, the precipitate was centrifuged and ultrasonically washed four times with deionized (DI) water. The obtained suspension can be stably re-dispersed in ethanol. GO nanosheets were prepared by a modified Hummer's method according to our previous study, and then dispersed in ethanol with a concentration of 5 mg mL⁻¹.¹⁴

The interconnected and well-aligned CNT scaffold was pulled out from a vertical CNT array, which was grown by chemical vapor deposition in a quartz tube furnace at 750 °C for 10 min. The areal density of the CNT scaffold was found to be ~2.12 μg cm⁻². Four layers of CNT films with a width of ~1.6 mm and a length of ~8 cm were first stacked onto a PTFE substrate. By measuring the area of the stacked CNT films, the mass of CNTs can be calculated, and the loading level of active materials in the fiber can be tuned by controlling the amount of Ni(OH)₂ ink. The Ni(OH)₂ nanosheets dispersed in ethanol with a concentration of 1 mg mL⁻¹ was drop-cast onto the CNT scaffold. Subsequently, the hybrid film was peeled off the PTFE substrate and scrolled into fiber with a motor rotating at 200 rpm for 2 min. The GO/CNT fiber was fabricated in a similar way and immersed in hydroiodic acid (HI, 55 wt%, Sigma Aldrich, ACS reagent) at room temperature for 12 h to reduce GO to form rGO/CNTs.

Similar to our previous study,¹⁴ solid-state fiber-based supercapacitors were fabricated and tested in a two-electrode configuration using the Ni(OH)₂/CNT and rGO/CNT fiber as the positive and negative electrode, respectively. PVA-KOH gel, which was prepared by mixing KOH (1 M, 10 mL) with PVA powder followed by heating at 90 °C with vigorous stirring, was used as the solid electrolyte. The hybrid device was sealed in a thermal plastic tube with a piece of nonwoven fabric as a separator. Ag paste applied at both ends of the fibers served as the conductive pads for electrochemical measurements.

Scanning electron microscopy (SEM) images were obtained on a field-emission scanning electron microscope (JEOL, JSM-6700F, Japan). Transmission electron spectroscopy (TEM) images were taken with a JEOL-2100F at an acceleration voltage of 200 kV. The phase analyses of the samples were performed by X-ray diffraction (XRD) on a Rigaku-Ultima III with Cu Kα radiation (λ = 1.5418 Å). N₂ adsorption-desorption isotherms of Ni(OH)₂ nanosheets were measured at 77 K using a Quantachrome Autosorb-6b static volumetric instrument. The samples were first degassed under high vacuum (<0.01 mbar). The specific surface area was calculated by the Brunauer-Emmett-Teller (BET) method. The electrical conductivity of fibers was measured in a two-probe configuration using a Keithley 2400. Ag paste was applied at both ends of the hybrid fibers for electrical wiring. The electrochemical measurements were obtained on a CHI 660D electrochemical workstation.

Ag/AgCl (saturated KCl) and Pt wire were used as a reference and counter electrode, respectively. The specific volumetric capacitance (C_v) and gravimetric capacitance (C_g) of the fiber electrodes were calculated from the galvanostatic charge-discharge curves according to the equation $C_v = [i/(dV/dt)]/V_{\text{fiber}}$ and $C_g = [i/(dV/dt)]/m_{\text{Ni(OH)}_2}$, where i is the discharge current, dV/dt is the slope of the discharge curve, and V_{fiber} and $m_{\text{Ni(OH)}_2}$ refer to the volume of the fiber electrode and the loading amount of Ni(OH)₂ nanosheets, respectively. The specific volumetric capacitance (C_v) of the fiber-based hybrid supercapacitor was calculated from the galvanostatic charge-discharge curves according to the equation $C_v = [i/(dV/dt)]/V_{\text{total}}$, where V_{total} refers to the total volume of two fibers.

Conflicts of interest

There are no conflicts to declare.

Acknowledgements

This work was supported by the National Natural Science Foundation of China (61704076 and 11674140), the Natural Science Foundation of Jiangsu Province (BK20171018), the NanjingTech Start-Up Grant (3983500150), the Jiangsu Specially-Appointed Professor program (54935012), and the Singapore Ministry of Education Academic Research Fund (AcRF) Tier 1: RG10/16 and RG111/15, and Tier 2: MOE2016-T2-2-004.

Notes and references

- 1 D. S. Yu, Q. H. Qian, L. Wei, W. C. Jiang, K. L. Goh, J. Wei, J. Zhang and Y. Chen, *Chem. Soc. Rev.*, 2015, **44**, 647–662.
- 2 W. Zeng, L. Shu, Q. Li, S. Chen, F. Wang and X. M. Tao, *Adv. Mater.*, 2014, **26**, 5310–5336.
- 3 H. Jang, Y. J. Park, X. Chen, T. Das, M. S. Kim and J. H. Ahn, *Adv. Mater.*, 2016, **28**, 4184–4202.
- 4 W. Weng, P. N. Chen, S. S. He, X. M. Sun and H. S. Peng, *Angew. Chem., Int. Ed.*, 2016, **55**, 6140–6169.
- 5 D. C. Zou, Z. B. Lv, X. Cai and S. C. Hou, *Nano Energy*, 2012, **1**, 273–281.
- 6 L. Li, P. P. Shi, L. Hua, J. N. An, Y. J. Gong, R. Y. Chen, C. Y. Yu, W. W. Hua, F. Xiu, J. Y. Zhou, G. F. Gao, Z. Jin, G. Z. Sun and W. Huang, *Nanoscale*, 2018, **10**, 118–123.
- 7 G. Z. Sun, X. Zhang, R. Z. Lin, B. Chen, L. X. Zheng, X. Huang, L. Huang, W. Huang, H. Zhang and P. Chen, *Adv. Electron. Mater.*, 2016, **2**, 1600102.
- 8 Y. Gao, L. W. Mi, W. T. Wei, S. Z. Cui, Z. Zheng, H. W. Hou and W. H. Chen, *ACS Appl. Mater. Interfaces*, 2015, **7**, 4311–4319.
- 9 X. Xiao, H. M. Yu, H. Y. Jin, M. H. Wu, Y. S. Fang, J. Y. Sun, Z. M. Hu, T. Q. Li, J. B. Wu, L. Huang, Y. Gogotsi and J. Zhou, *ACS Nano*, 2017, **11**, 2180–2186.

- 10 M. H. Yu, X. Y. Cheng, Y. X. Zeng, Z. L. Wang, Y. X. Tong, X. H. Lu and S. H. Yang, *Angew. Chem., Int. Ed.*, 2016, **55**, 6762–6766.
- 11 S. Gu, Z. Lou, X. Ma and G. Shen, *ChemElectroChem*, 2015, **2**, 1042–1047.
- 12 H. Y. Jin, L. M. Zhou, C. L. Mak, H. T. Huang, W. M. Tang and H. L. W. Chan, *Nano Energy*, 2015, **11**, 662–670.
- 13 Y. N. Meng, Y. Zhao, C. G. Hu, H. H. Cheng, Y. Hu, Z. P. Zhang, G. Q. Shi and L. T. Qu, *Adv. Mater.*, 2013, **25**, 2326–2331.
- 14 G. Z. Sun, X. Zhang, R. Z. Lin, J. Yang, H. Zhang and P. Chen, *Angew. Chem., Int. Ed.*, 2015, **54**, 4651–4656.
- 15 D. Yu, K. Goh, Q. Zhang, L. Wei, H. Wang, W. Jiang and Y. Chen, *Adv. Mater.*, 2014, **26**, 6790–6797.
- 16 J. Yu, W. Lu, J. P. Smith, K. S. Booksh, L. Meng, Y. Huang, Q. Li, J. H. Byun, Y. Oh and Y. Yan, *Adv. Energy Mater.*, 2017, **7**, 1600976.
- 17 Z. Gao, C. Bumgardner, N. N. Song, Y. Y. Zhang, J. J. Li and X. D. Li, *Nat. Commun.*, 2016, **7**, 11586.
- 18 Z. M. Hu, X. Xiao, H. Y. Jin, T. Q. Li, M. Chen, Z. Liang, Z. F. Guo, J. Li, J. Wan, L. Huang, Y. R. Zhang, G. Feng and J. Zhou, *Nat. Commun.*, 2017, **8**, 15630.
- 19 P. H. Yang, X. Xiao, Y. Z. Li, Y. Ding, P. F. Qiang, X. H. Tan, W. J. Mai, Z. Y. Lin, W. Z. Wu, T. Q. Li, H. Y. Jin, P. Y. Liu, J. Zhou, C. P. Wong and Z. L. Wang, *ACS Nano*, 2013, **7**, 2617–2626.
- 20 J. Y. Zhou, H. Zhao, X. M. Mu, J. Y. Chen, P. Zhang, Y. L. Wang, Y. M. He, Z. X. Zhang, X. J. Pan and E. Q. Xie, *Nanoscale*, 2015, **7**, 14697–14706.
- 21 X. H. Lu, T. Zhai, X. H. Zhang, Y. Q. Shen, L. Y. Yuan, B. Hu, L. Gong, J. Chen, Y. H. Gao, J. Zhou, Y. X. Tong and Z. L. Wang, *Adv. Mater.*, 2012, **24**, 938–944.
- 22 D. Y. Zhang, Y. H. Zhang, Y. S. Luo and P. K. Chu, *Nano Energy*, 2015, **13**, 47–57.
- 23 W. J. Zhou, K. Zhou, X. J. Liu, R. Z. Hu, H. Liu and S. W. Chen, *J. Mater. Chem. A*, 2014, **2**, 7250–7255.
- 24 C. Choi, J. A. Lee, A. Y. Choi, Y. T. Kim, X. Lepro, M. D. Lima, R. H. Baughman and S. J. Kim, *Adv. Mater.*, 2014, **26**, 2059–2065.
- 25 N. Yu, H. Yin, W. Zhang, Y. Liu, Z. Tang and M. Q. Zhu, *Adv. Energy Mater.*, 2016, **6**, 1501458.
- 26 W. T. Wei, S. Z. Cui, L. Y. Ding, L. W. Mi, W. H. Chen and X. L. Hu, *ACS Appl. Mater. Interfaces*, 2017, **9**, 40655–40670.
- 27 C. Choi, K. M. Kim, K. J. Kim, X. Lepro, G. M. Spinks, R. H. Baughman and S. J. Kim, *Nat. Commun.*, 2016, **7**, 13811.
- 28 P. P. Shi, L. Li, L. Hua, Q. Q. Qian, P. F. Wang, J. Y. Zhou, G. Z. Sun and W. Huang, *ACS Nano*, 2017, **11**, 444–452.
- 29 L. L. Zhang and X. S. Zhao, *Chem. Soc. Rev.*, 2009, **38**, 2520–2531.
- 30 J. X. Zhu, D. Yang, Z. Y. Yin, Q. Y. Yan and H. Zhang, *Small*, 2014, **10**, 3480–3498.
- 31 K. Wang, Q. H. Meng, Y. J. Zhang, Z. X. Wei and M. H. Miao, *Adv. Mater.*, 2013, **25**, 1494–1498.
- 32 Q. Q. Qian, Q. Hu, L. Li, P. P. Shi, J. Y. Zhou, J. M. Kong, X. J. Zhang, G. Z. Sun and W. Huang, *Sens. Actuators, B*, 2018, **257**, 23–28.
- 33 L. Hua, Z. Y. Ma, P. P. Shi, L. Li, K. Rui, J. Y. Zhou, X. Huang, X. Liu, J. X. Zhu, G. Z. Sun and W. Huang, *J. Mater. Chem. A*, 2017, **5**, 2483–2487.
- 34 W. T. Wei, L. W. Mi, Y. Gao, Z. Zheng, W. H. Chen and X. X. Guan, *Chem. Mater.*, 2014, **26**, 3418–3426.
- 35 W. T. Wei, W. H. Chen, L. Y. Ding, S. Z. Cui and L. W. Mi, *Nano Res.*, 2017, **10**, 3726–3742.
- 36 F. Zou, X. L. Hu, Z. Li, L. Qie, C. C. Hu, R. Zeng, Y. Jiang and Y. H. Huang, *Adv. Mater.*, 2014, **26**, 6622–6628.
- 37 Y. X. Zeng, Y. Meng, Z. Z. Lai, X. Y. Zhang, M. H. Yu, P. P. Fang, M. M. Wu, Y. X. Tong and X. H. Lu, *Adv. Mater.*, 2017, **29**, 1702698.
- 38 Y. X. Zeng, X. Y. Zhang, Y. Meng, M. H. Yu, J. N. Yi, Y. Q. Wu, X. H. Lu and Y. X. Tong, *Adv. Mater.*, 2017, **29**, 1700274.
- 39 M. D. Lima, S. L. Fang, X. Lepro, C. Lewis, R. Ovalle-Robles, J. Carretero-Gonzalez, E. Castillo-Martinez, M. E. Kozlov, J. Y. Oh, N. Rawat, C. S. Haines, M. H. Haque, V. Aare, S. Stoughton, A. A. Zakhidov and R. H. Baughman, *Science*, 2011, **331**, 51–55.
- 40 R. Chen, G. Z. Sun, C. J. Yang, L. P. Zhang, J. W. Miao, H. B. Tao, H. B. Yang, J. Z. Chen, P. Chen and B. Liu, *Nanoscale Horiz.*, 2016, **1**, 156–160.
- 41 G. Z. Sun, J. Q. Liu, L. X. Zheng, W. Huang and H. Zhang, *Angew. Chem., Int. Ed.*, 2013, **52**, 13351–13355.
- 42 G. Z. Sun, L. X. Zheng, J. An, Y. Z. Pan, J. Y. Zhou, Z. Y. Zhan, J. H. L. Pang, C. K. Chua, K. F. Leong and L. Li, *Nanoscale*, 2013, **5**, 2870–2874.
- 43 G. Z. Sun, Y. X. Huang, L. X. Zheng, Z. Y. Zhan, Y. N. Zhang, J. H. L. Pang, T. Wu and P. Chen, *Nanoscale*, 2011, **3**, 4854–4858.
- 44 D. A. Corrigan and R. M. Bendert, *J. Electrochem. Soc.*, 1989, **136**, 723–728.
- 45 F. S. Cai, G. Y. Zhang, J. Chen, X. L. Gou, H. K. Liu and S. X. Dou, *Angew. Chem., Int. Ed.*, 2004, **43**, 4212–4216.
- 46 J. T. Li, W. Zhao, F. Q. Huang, A. Manivannan and N. Q. Wu, *Nanoscale*, 2011, **3**, 5103–5109.
- 47 C.-G. Liu, Y.-S. Lee, Y.-J. Kim, I.-C. Song and J.-H. Kim, *Synth. Met.*, 2009, **159**, 2009–2012.
- 48 H. Wang, H. S. Casalongue, Y. Liang and H. Dai, *J. Am. Chem. Soc.*, 2010, **132**, 7472–7477.
- 49 J. W. Lee, T. Ahn, D. Soundararajan, J. M. Ko and J.-D. Kim, *Chem. Commun.*, 2011, **47**, 6305–6307.
- 50 C. Choi, K. M. Kim, K. J. Kim, X. Lepro, G. M. Spinks, R. H. Baughman and S. J. Kim, *Nat. Commun.*, 2016, **7**, 13811.
- 51 D. S. Yu, K. Goh, H. Wang, L. Wei, W. C. Jiang, Q. Zhang, L. M. Dai and Y. Chen, *Nat. Nanotechnol.*, 2014, **9**, 555–562.
- 52 J. A. Lee, M. K. Shin, S. H. Kim, H. U. Cho, G. M. Spinks, G. G. Wallace, M. D. Lima, X. Lepro, M. E. Kozlov, R. H. Baughman and S. J. Kim, *Nat. Commun.*, 2013, **4**, 1970.
- 53 L. Kou, T. Q. Huang, B. N. Zheng, Y. Han, X. L. Zhao, K. Gopalsamy, H. Y. Sun and C. Gao, *Nat. Commun.*, 2014, **5**, 3754.

- 54 H. F. Ju, W. L. Song and L. Z. Fan, *J. Mater. Chem. A*, 2014, **2**, 10895–10903.
- 55 M. F. El-Kady and R. B. Kaner, *Nat. Commun.*, 2013, **4**, 1475.
- 56 D. Pech, M. Brunet, H. Durou, P. H. Huang, V. Mochalin, Y. Gogotsi, P. L. Taberna and P. Simon, *Nat. Nanotechnol.*, 2010, **5**, 651–654.
- 57 X. Xiao, T. Q. Li, P. H. Yang, Y. Gao, H. Y. Jin, W. J. Ni, W. H. Zhan, X. H. Zhang, Y. Z. Cao, J. W. Zhong, L. Gong, W. C. Yen, W. J. Mai, J. Chen, K. F. Huo, Y. L. Chueh, Z. L. Wang and J. Zhou, *ACS Nano*, 2012, **6**, 9200–9206.
- 58 A. D. Jagadale, G. Guan, X. Li, X. Du, X. Ma, X. Hao and A. Abudula, *Energy Technol.*, 2016, **4**, 997–1004.
- 59 X. L. Dong, Z. Y. Guo, Y. F. Song, M. Y. Hou, J. Q. Wang, Y. G. Wang and Y. Y. Xia, *Adv. Funct. Mater.*, 2014, **24**, 3405.
- 60 P. P. Shi, R. Chen, L. Hua, L. Li, R. Y. Chen, Y. J. Gong, C. Y. Yu, J. Y. Zhou, B. Liu, G. Z. Sun and W. Huang, *Adv. Mater.*, 2017, **25**, 1703455.